Singlet versus Triplet Reactivity in an Mn(V)−Oxo Species: Testing Theoretical Predictions Against Experimental Evidence

Tzuhsiung Yang,[†] Matthew G. Quesne,[‡,§] Heather M. Neu,[†] Fabián G. Cantú Reinhard,[‡] David P. Goldberg,*[,†] and Sam P. de Visser*[,‡]

[†]Department of Chemistry, The Johns Hopkins University, Baltimore, Maryland 21218, United States
[‡]Manchester Institute of Biotechnology and School of Chemical Engineering and Analytical Science, The University of Manchester, 131 Princess Street, Manchester M1 7DN, United Kingdom

Ⓢ Supporting Information

ABSTRACT: Discerning the factors that control the reactivity of high-valent metal−oxo species is critical to both an understanding of metalloenzyme reactivity and related transition metal catalysts. Computational studies have suggested that an excited higher spin state in a number of metal−oxo species can provide a lower energy barrier for oxidation reactions, leading to the conclusion that this unobserved higher spin state complex should be considered as the active oxidant. However, testing these computational predictions by experiment is difficult and has rarely been accomplished. Herein, we describe a detailed computational study on the role of spin state in the reactivity of a high-valent manganese(V)−oxo complex with para-Z-substituted

singlet spin reactivity

thioanisoles and utilize experimental evidence to distinguish between the theoretical results. The calculations show an unusual change in mechanism occurs for the dominant singlet spin state that correlates with the electron-donating property of the para-Z substituent, while this change is not observed on the triplet spin state. Minimum energy crossing point calculations predict small spin−orbit coupling constants making the spin state change from low spin to high spin unlikely. The trends in reactivity for the para-Z-substituted thioanisole derivatives provide an experimental measure for the spin state reactivity in manganese−oxo corrolazine complexes. Hence, the calculations show that the V-shaped Hammett plot is reproduced by the singlet surface but not by the triplet state trend. The substituent effect is explained with valence bond models, which confirm a change from an electrophilic to a nucleophilic mechanism through a change of substituent.
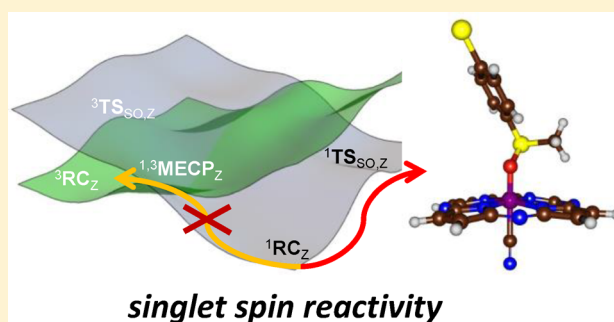
■ INTRODUCTION

Metal−oxo complexes are proposed to be the active species in enzyme-catalyzed water oxidation, energy utilization, drug metabolism, and many other vital functions of organisms.[1] One particular class of enzymes with great relevance to biocatalysis and biodegradation are the cytochromes P450, which in the human body have functions that give them their primary purpose in the metabolism of harmful xenobiotics (drugs), as well as in the synthesis of hormones.[2] These enzymes form a high-valent iron(IV)−oxo heme cation radical as the active oxidant that performs a versatile set of reactions efficiently.[3] While metal−oxo complexes are generally thought to reside in their lower spin states in these hexacoordinated heme structures, actually the iron(IV)−oxo species in pentacoordinated nonheme enzymes typically exhibits a high-spin state.[4] It has been argued that the spin state of the metal−oxo oxidants determines its reactivity pattern with substrates.[5]

Over the years a range of biomimetic model complexes have been designed that mimic the active features of enzymatic systems.[6] A number of the former studies characterized an active metal−oxo oxidant, which is often found in an intermediate-spin iron(IV)−oxo or low-spin manganese(V)−

oxo state.[7,8] It has been proposed from computational studies that in many cases the active species that reacts with substrates is, in fact, an excited high-spin state of the metal−oxo species generated from spin crossover from the lower spin ground state.[9] This proposal arises because the excited high-spin state is often calculated to give a lower energy barrier for the activation of substrates, providing a possible faster reaction pathway.

Experimental methods to test these computational predictions are rare. Recent work on C−H activation by nonheme Fe[IV](O) complexes has shown that experimental kinetic isotope effects (KIEs) can serve as a potential probe for the reactive spin state of iron−oxo species.[10] For example, very large, nonclassical KIEs observed for the C−H activation reactions of two nonheme Fe[IV](O) complexes matched calculations for the lower $S = 1$ Fe[IV](O) spin state but did not fit for the higher $S = 2$ excited state. It was concluded that reactivity occurred along the $S = 1$ spin state pathway, even though the quintet state was calculated to yield a lower reaction barrier.[10c] Although this recent analysis of observable KIEs has provided some

experimental measure of spin state reactivity correlations for C−H activation, an experimental test regarding spin state reactivity in the other major class of biomimetic oxidations, oxygen-atom-transfer reactions, has yet to be described. In addition, there are no reports, to our knowledge, discussing direct experimental evidence that can distinguish between possible reactive spin states in high-valent manganese−oxo, as opposed to iron−oxo, complexes.

Particularly useful for the studies of manganese(V)−oxo complexes are the porphyrinoid ligand systems corrole and corrolazine,[8,11] which are able to stabilize metals in high oxidation states. Work of our groups established that a low-spin manganese(V)−oxo porphyrinoid complex $[Mn^V(O)-(TBP_8Cz)]$, TBP_8Cz = octakis(p-tertbutylphenyl) corrolazinato[3−], underwent a drastic rate enhancement in hydrogen-atom abstraction reactivity upon the addition of anionic axial ligands (X^-) such as cyanide or fluoride.[12] In a separate computational study, our conclusions regarding this low-spin $Mn^V(O)$ reactivity were questioned, and it was suggested that the reactant state had a close-lying triplet spin conformation that was more likely the reactive state.[13] A similarly large increase in reactivity for oxygen-atom-transfer (OAT) reactions was seen upon addition of X^- to $[Mn^V(O)(TBP_8Cz)]$ and reported in two separate studies.[14] In one of these studies, $[Mn^V(O)-(TBP_8Cz)(CN)]^-$ was reacted with derivatives of seven para-Z-substituted thioanisoles, and a Hammett analysis involving the measure of reaction rates versus the σ_P Hammett parameter of the para-Z substituent was conducted (lower part of Scheme 1).[14a] The obtained plot shows a surprising V-shaped pattern,
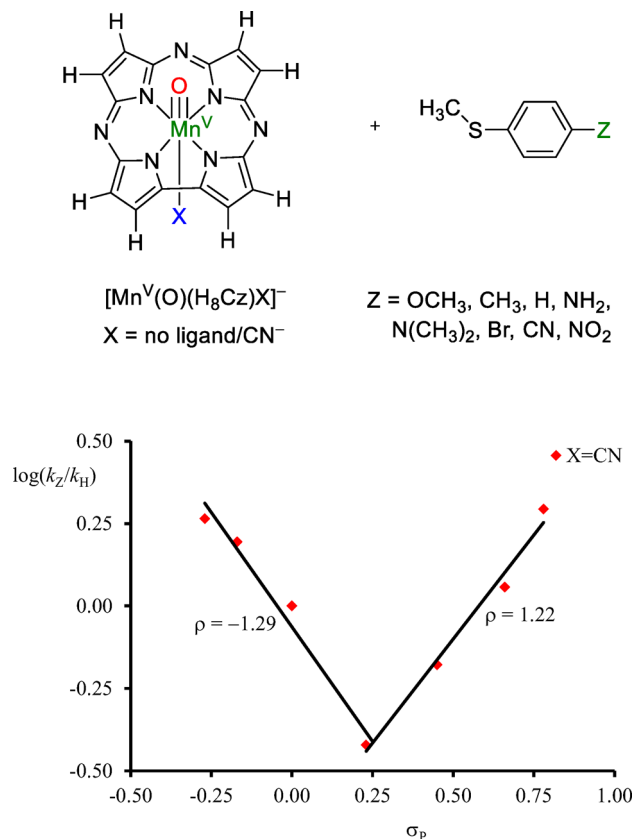
whereby a negative slope is observed for electron-donating substituents but a positive slope is seen for electron-withdrawing substituents. This observation was explained by differences in reaction mechanism, in which the former substrates reacted through an electrophilic pathway while the latter substrates reacted through a nucleophilic pathway. However, the role of spin state in these OAT reactions and, in particular, the unusual V-shaped Hammett plot was not examined in this earlier work.
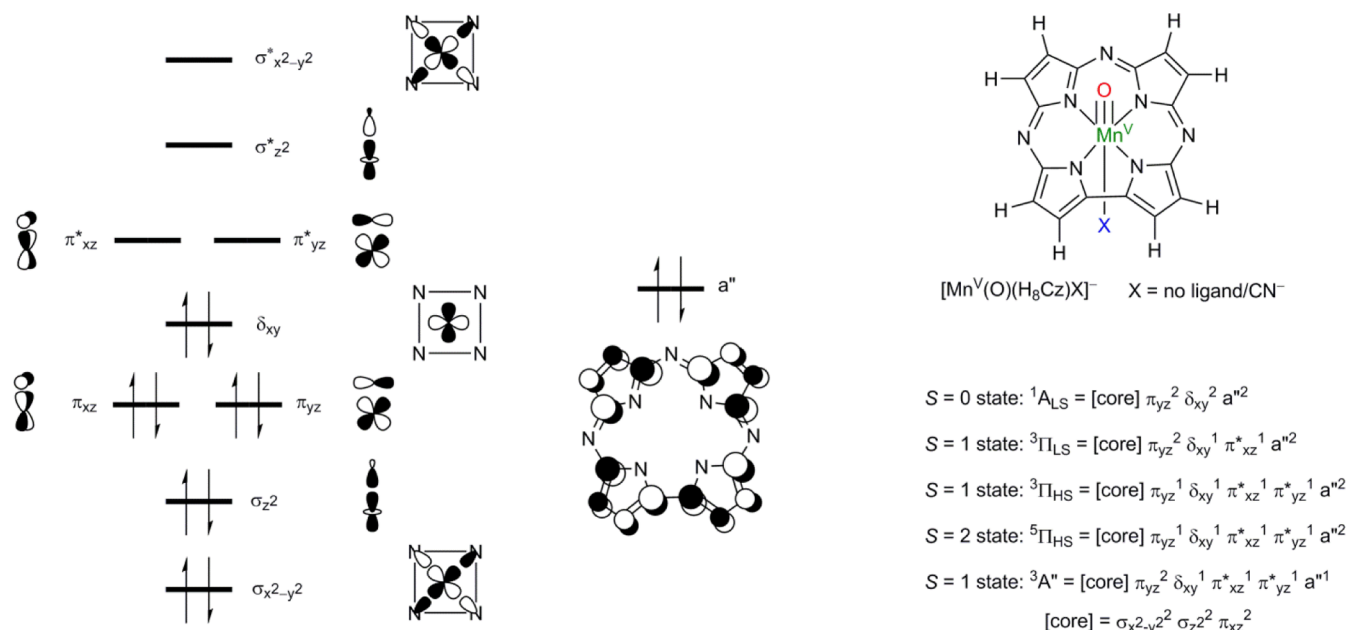
Herein, we describe a detailed density functional theory (DFT) and ab initio study on the spin state reactivity of $[Mn(O)(H_8Cz)(CN)]^-$ with para-Z-substituted thioanisole substrates whereby we expanded the substrate range to eight substrates (top part of Scheme 1). This study shows that the V-shaped Hammett plot provides a direct, experimental measure of the reactive spin state pathway for OAT in a high-valent manganese−oxo complex. The experimental and computational findings point to direct sulfoxidation on a dominant low-spin singlet pathway, even though an excited state triplet pathway provides an apparent lower reaction barrier. The experimentally determined Hammett plot for p-Z-thioanisole sulfoxidation by $[Mn^V(O)(TBP_8Cz)(CN)]^-$ provides, to our knowledge, the first experimental evidence of singlet spin reactivity and the lack of spin crossing to a higher spin state surface in a high-valent manganese−oxo complex.

■ METHODS

Calculations were performed using the Orca (version 3.0.3) and Gaussian-09 computational chemistry software packages.[15] Our model uses a corrolazine macrocycle (Scheme 1) with the peripheral aryl substituents replaced with hydrogen atoms (H_8Cz), as previous work showed that the peripheral groups on porphyrin scaffolds have little influence on the spin state ordering and relative energies.[16] Reactivities with para-Z-substituted thioanisoles were calculated for Z = $N(CH_3)_2$, NH_2, OCH_3, CH_3, H, Br, CN, and NO_2. The work was aimed at establishing whether the reaction mechanisms are electrophilic or nucleophilic and how the intrinsic chemical properties of oxidant and substrate affected these reactivity differences. The nature of all transition states, in particular, the singlet spin transition states, was established (i) through frequency calculations that gave a single imaginary mode for the S−O bond formation and (ii) intrinsic reaction coordinate (IRC) scans in both the forward and the reverse directions. The latter unequivocally connected the transition states to the reactants in one direction and to products in the opposite direction.

Enthalpies of activation of the chemical reactions are compared to experimental data reported previously.[14a] However, it should be noted that generally gas-phase calculations overestimate the entropy of activation and often find higher values than experiment. As such, previous experience of calibrating oxygen transfer reactivities against low-pressure gas-phase measured rate constants gave a better correlation with enthalpies of activation,[17] which we will adopt here.

All initial geometry optimizations (including transition state geometry optimizations) were performed without constraints and used the hybrid generalized gradient approximation (GGA) functional B3LYP that includes the VWN5 local density approximation.[18] Relativistic small effective core potential basis sets SDD or LACVP were used on Mn and the all-electron 6-31G(d) on the rest of atoms: basis set BS1.[19] Long-range dispersion interactions were applied using the D3 procedure of Grimme et al.[20] Geometry optimizations were followed by a frequency calculation at the same level of theory and confirmed all structures as local minima or first-order saddle points (transition states). Using Orca, energies were calculated from single-point calculations at the UB3LYP/BS1-optimized geometries using a correlation-consistent basis set of def2-QZVPP on Mn and cc-pVDZ on the rest of the atoms: basis set BS2. The resolution of identity (RI) approximation to the Coulomb integrals was used with corresponding

Scheme 1. Structure of Complexes and Substrates Investigated, and Experimental Hammett Plot with Data Taken from Ref 14a

$[Mn^V(O)(H_8Cz)X]^-$
X = no ligand/CN^-

Z = OCH_3, CH_3, H, NH_2,
$N(CH_3)_2$, Br, CN, NO_2

Scheme 2. High-Lying Occupied and Virtual Molecular Orbitals of $[Mn(O)(H_8Cz)(CN)]^-$ and Occupation Levels in Various Electronic States

$[Mn^V(O)(H_8Cz)X]^-$ X = no ligand/CN^-

$S = 0$ state: $^1A_{LS} = $ [core] $\pi_{yz}^2\, \delta_{xy}^2\, a''^2$

$S = 1$ state: $^3\Pi_{LS} = $ [core] $\pi_{yz}^2\, \delta_{xy}^1\, \pi^*_{xz}^1\, a''^2$

$S = 1$ state: $^3\Pi_{HS} = $ [core] $\pi_{yz}^1\, \delta_{xy}^1\, \pi^*_{xz}^1\, \pi^*_{yz}^1\, a''^2$

$S = 2$ state: $^5\Pi_{HS} = $ [core] $\pi_{yz}^1\, \delta_{xy}^1\, \pi^*_{xz}^1\, \pi^*_{yz}^1\, a''^2$

$S = 1$ state: $^3A'' = $ [core] $\pi_{yz}^2\, \delta_{xy}^1\, \pi^*_{xz}^1\, \pi^*_{yz}^1\, a''^1$

[core] $= \sigma_{x^2-y^2}^2\, \sigma_{z^2}^2\, \pi_{xz}^2$

auxiliary basis sets, as implemented in Orca. The integration grid was increased from 3 to 4 (Orca notation) to increase numerical accuracy. Single-point energy calculations on all optimized structures were also performed using the hybrid meta-GGA functional TPSSh with 10% HF exchange and the D3 dispersion correction.[20,21] A similar protocol was followed for the results obtained using the Gaussian software program, although it uses the VWN3 local density approximation in B3LYP; furthermore, these calculations utilized the triple-ζ quality LACV3P+* on Mn (with core potential) and 6-311+G* on the rest of the atoms: basis set BS3. Generally, these studies confirmed the B3LYP obtained landscape and conclusions and did not deviate significantly. Solvent effects were included in Orca by applying the conductor-like screening model (COSMO) with a dielectric constant of 26.0 and probe radius of 1.528 Å mimicking benzonitrile.[22] An implicit solvent correction in Gaussian was included using the polarized continuum model (CPCM) with a dielectric constant of ε = 35.688 mimicking acetonitrile.

To test the accuracy and reproducibility of the density functional methods, a range of test calculations with alternative density functional methods and the def2-TZVPP basis set (BS4) were performed, including BP86,[23] BLYP,[18b,23a] PBE,[24] B3LYP,[18] PBE0,[25] and TPSSh.[21] In addition, the spin state ordering of the $[Mn(O)(H_8Cz)-(CN)]^-$ complex was investigated using the complete active space self-consistent field (CASSCF) methods in Orca. Dynamic correlation was recovered by following these CASSCF studies with the N-electron valence second-order perturbation theory (NEVPT2) correction on the converged multiconfigurational wave functions with basis set BS5 (cc-pVTZ/cc-pVDZ). Due to the size of our chemical system, the NEVPT2:CAS studies were performed at the single-point energy level on the UB3LYP/BS1-optimized geometries of the reactant complexes only. The resolution of identity approximation and the chain-of-sphere approximation (RIJCOSX) were applied to the Coulomb and exchange correlation, respectively, with density fitting auxiliary basis set corresponding to each atomic basis set throughout the calculations below.

Single-point energies were calculated on the triplet spin state of the optimized singlet spin transition state geometry using B3LYP. The ZORA Hamiltonian with the model potential due to Van Wuellen[26] was used to account for the relativistic effect along with the segmented all-electron relativistically recontracted version of basis sets def2-TZVPP.[27] The Ahlrichs (2df,2pd) polarization functions were obtained from the Turbomole basis set library[28] for Mn, while the

def2-SVP basis set[27] was employed on the rest of atoms. The resolution of identity (RI) and the chain-of-sphere approximations were used for the Coulomb and Exchange correlation, respectively. Spin−orbit coupling constants (SOC) were calculated on the converged unrestricted natural orbitals using the spin−orbit mean field Hamiltonian including 1-electron term and local DFT correlation including VWN5.[29] Coulomb terms were computed with the RI approximation, and the exchange terms were computed with one-center exact integrals including the spin−orbit interaction.

RESULTS AND DISCUSSION

Density functional theory (DFT) methods sometimes struggle with the correct description and spin state ordering of transition metal complexes, in particular of manganese complexes.[30] In this work a series of test calculations were performed with a variety of density functional and ab initio methods, and the results were compared with experimental (spectroscopic) data. It should be noted that computational methods that better reproduce experimental crystal structure coordinates are often not the preferred methods for reproducing reaction rates, as found previously.[31] We undertook an extensive benchmarking study of the $[Mn(O)(H_8Cz)-(CN)]^-$ complex using a range of density functional and ab initio methods, particularly aimed at establishing the amount of Hartree−Fock exchange interaction needed in the calculations.

Optimized geometries were compared against the reported structural parameters from X-ray absorption spectroscopy (XAS) published previously[14a] and calculated using a variety of density functional methods. A detailed overview of these results is given in the Supporting Information (Tables S1−S4). In general, the results lead to the conclusion that the BLYP and TPSS density functional methods perform consistently better than alternative pure density functional methods for matching the metrical parameters obtained from XAS (Table S1, Supporting Information). TPSS performed slightly better than BLYP, as expected according to the Jacob's ladder scheme.[32] Among all three hybrid density functional methods, B3LYP performed the best except in Median Absolute Deviation. B3LYP performs better than TPSSh for two reasons:

Table 1. Calculated Adiabatic Singlet-Triplet Energy Gaps (ΔE_{ST}) and Unpaired Spin Density in the Triplet Spin State of [Mn(O)(H$_8$Cz)(CN)]$^-$ Using a Range of Density Functional Methods and Basis Set BS2 on Different Optimized Geometries[a,b]

geometry	BP86	BLYP	PBE	TPSS	B3LYP	PBE0	TPSSh
BLYP[c]	9.15 (2.13)	9.48 (2.08)	9.14 (2.12)	8.78 (2.11)	1.84 (3.05)	−3.87 (3.44)	5.25 (2.62)
TPSS[d]	9.23 (2.12)	9.41 (2.06)	9.21 (2.11)	8.83 (2.10)	2.15 (3.03)	−3.26 (3.43)	5.47 (2.63)
B3LYP[e]	15.37 (2.77)	14.45 (2.55)	15.48 (2.69)	13.58 (3.07)	0.69 (3.79)	−6.51 (3.99)	6.74 (3.64)

[a]Relative energies in kcal mol^{-1}; a positive value denotes a singlet spin ground state. [b]Total unpaired spin density is given in parentheses as the sum of the absolute values of Mn and O. [c]Calculated Mn−O distances of 1.59 (singlet) and 1.66 (triplet) Å. [d]Calculated Mn−O distances of 1.58 (singlet) and 1.66 (triplet) Å. [e]Calculated Mn−O distances of 1.55 (singlet) and 1.78 (triplet) Å.

(1) B3LYP contains a larger amount of HF exchange and (2) has a better parametrized correlation functional. On the basis of these results, therefore, we continued the studies with hybrid density functional methods only. The effective core potential-all electron basis set combination SDD/6-31G(d) excelled compared to the other two combinations tested in agreement with previous findings.[33]

Spin State Ordering and Electronic Ground State of [Mn(O)(H$_8$Cz)(CN)]$^-$. It is sometimes difficult to calculate excited states and spin state ordering by DFT, because it is formally a ground-state theory. As a consequence, different density functional methods can give inconsistent results, especially for transition metal complexes where near-degeneracy of the d orbitals poses a difficulty for this single-determinant theory.[30] The exchange-correlation term is different for each density functional method, and its value determines the energy associated with electron pairing. Therefore, the correct choice of DFT method influences the obtained results and is extremely important in determining spin state ordering, where many close-lying spin states are present.

Indeed, Shaik and co-workers previously demonstrated that the spin state ordering of [Mn(O)(H$_8$Cz)] could vary greatly with different exchange-correlation functionals and/or the amount of HF exchange included.[13] They also suggested that the spin ground state of [Mn(O)(H$_8$Cz)(CN)]$^-$ should be the triplet spin state as opposed to the experimentally determined singlet spin state of the parent five-coordinate complex. To highlight the spin accessibility and the electronic possibilities of the [Mn(O)(H$_8$Cz)(CN)]$^-$ reactant complex, we show high-lying occupied and low-lying virtual orbitals in Scheme 2.

The metal orbitals form bonding and antibonding combinations with orbitals on the first coordination sphere ligands. In the xy plane, the $3d_{x^2-y^2}$ orbital on Mn mixes with $2p\sigma$ orbitals on the nitrogen atoms of the corrolazine ring to give the $\sigma_{x^2-y^2}/\sigma^*_{x^2-y^2}$ pair of orbitals, whereas the nonbonding δ_{xy} orbital lies in between the nitrogen atoms. Along the z axis, the $3d_{z^2}$ orbital on Mn mixes with the $2p\sigma$ orbital of oxygen to form the $\sigma_{z^2}/\sigma^*_{z^2}$ orbitals, whereas the $3d_{xz}/3d_{yz}$ orbitals form π-type interactions with the $2p_x/2p_y$ orbitals to give the π_{xz}/π^*_{xz} and π_{yz}/π^*_{yz} pair of orbitals. In addition, there are several high-lying π orbitals on the corrolazine ligand, and the a″ shape is shown in Scheme 2. This highly dispersed orbital shows similarity to the a$_{1u}$ orbital in heme structures.[34] The experimental evidence indicates a closed-shell singlet ground state (^{1}A$_{LS}$) for manganese(V)−oxo corrolazine complexes. However, the a″ orbital can become singly occupied through valence tautomerism upon binding of a Lewis acid such as Zn^{2+} to the oxo ligand, stabilizing a ^{3}A″ electronic state.[35] These findings suggest that the orbital manifold is close in energy and various ground states could be accessible dependent on the local environmental conditions.

In the closed-shell singlet spin state (^{1}A$_{LS}$) these sets of orbitals are occupied as [core] $\pi_{yz}^2\delta_{xy}^2$ with [core] = $\sigma_{x^2-y^2}^2\sigma_{z^2}^2\pi_{xz}^2$, and all orbitals are in a low-spin (LS) configuration. The triplet spin state that retains the +5 oxidation state on Mn has occupation [core] $\pi_{yz}^2\delta_{xy}^1\pi^*_{xz}^1$ ($^3\Pi_{LS}$) and can be described as a high-spin Mn^V species. The alternative triplet spin state with four unpaired electrons (in high-spin configuration, $^3\Pi_{HS}$) is different, arising from promotion of an electron from π_{yz} to π^*_{yz}, and can be described as high-spin Mn^{IV} antiferromagnetically coupled with an oxyl radical (Mn^{IV}=O$^•$).

As the three electronic states (^{1}A$_{LS}$, $^3\Pi_{LS}$, and $^3\Pi_{HS}$) of [Mn(O)(H$_8$Cz)(CN)]$^-$ are expected to be close in energy we decided to investigate their spin state ordering and relative energies using various computational models. Although we attempted to characterize the ^{3}A″ as well, which would represent an Mn^{IV} π-cation−radical configuration, it was not low enough in energy for any of the systems examined to play a key role in reactivity. The results obtained for the DFT methods are summarized in Table 1, while raw data can be found in Tables S1−S5 (Supporting Information). Thus, the [Mn(O)(H$_8$Cz)(CN)]$^-$ complex was optimized in the singlet and triplet spin states using BLYP, TPSS, and B3LYP methods. The pure density functionals (BLYP and TPSS) give almost identical geometries with a short Mn−O distance below 1.6 Å in the singlet spin state that implicates a Mn−O triple bond. By contrast, due to additional antibonding character through occupation of the π^*_{xz} orbital in the triplet spin state the Mn−O distance is elongated to 1.66 Å. At the B3LYP level of theory, the singlet spin state has a shorter Mn-O distance of 1.55 Å, while the triplet state has a larger one of 1.78 Å. The group spin densities and orbital occupations, however, show that the B3LYP optimization led to the $^3\Pi_{HS}$ state, whereas the pure density functionals gave the $^3\Pi_{LS}$ state instead. As a consequence of occupation of an extra π^* orbital in the $^3\Pi_{HS}$ state the Mn−O distances are significantly elongated as compared to those in the $^3\Pi_{LS}$ state. In principle, the $^3\Pi_{HS}$ state has two singly occupied π^* orbitals for the MnO interaction, which would result in significant oxyl radical character. By contrast, in the $^3\Pi_{LS}$ state only one π^* orbital is singly occupied and the oxyl character will be significantly less than in the $^3\Pi_{HS}$ state.

In order to obtain an accurate value of the singlet−triplet energy gap and the nature of the lowest triplet spin configuration, we decided to study this chemical system with a method that allows accurate description of multiconfigurational systems, namely, the complete active space self-consistent field (CASSCF) method followed by the N-electron valence state second-order perturbation theory (NEVPT2) that accounts for dynamic correlation. The CASSCF calculations utilized either an active space of eight electrons in seven molecular orbitals or 12 electrons in 11 molecular orbitals, i.e.,

CAS(8,7) or CAS(12,11). The smallest CAS space contained the three oxygen 2p orbitals and four manganese 3d orbitals ($3d_{xz}$, $3d_{yz}$, $3d_{x2-y2}$, and $3d_{z2}$), whereas the larger CAS space included also the HOMO−1, HOMO, LUMO, and LUMO+1 orbitals on the H_8Cz moiety. Due to the size of the chemical system, we were unable to do a geometry optimization at the NEVPT2:CAS level of theory and consequently ran single points on DFT-optimized geometries (either B3LYP or BLYP) only.

Table 2 gives NEVPT2:CAS calculated singlet−triplet energy splitting as well as the unpaired spin population from CASSCF

Table 2. Spin State Energies between the Singlet and Triplet States of $[Mn(O)(H_8Cz)(CN)]^-$ As Calculated with NEVPT2:CAS/BS5 on Optimized DFT Geometries[a]

active space	geometry[b]	ΔE_{ST}[c]	$\rho(Mn)$	$\rho(O)$
(8,7)	BLYP	8.0	2.17	−0.21
(12,11)	BLYP	8.1	2.17	−0.20
(8,7)	B3LYP	9.9	2.40	−0.44
(12,11)	B3LYP	8.8	2.40	−0.43

[a]Unpaired spin densities on Mn and O are also given. [b]Singlet spin geometries have r_{MnO} = 1.59 Å for BLYP and 1.55 Å for B3LYP, and triplet spin geometries use r_{MnO} = 1.66 Å for BLYP and 1.78 Å for B3LYP. [c]In kcal/mol.

on the MnO group. In agreement with the DFT results (except PBE0) from Table 1, the singlet spin state is the ground state and well lower in energy than the triplet spin state. The result of the larger CAS(12,11) calculation is almost identical to that found for the CAS(8,7), with the triplet spin state about 8 kcal mol^{-1} higher in energy. Therefore, the high-lying occupied and low-lying virtual corrolazine orbitals had little contribution to the singlet−triplet splitting. In addition, the radical character in the triplet spin states implicates a situation closest to the $^3\Pi_{LS}$ state with two unpaired electrons in δ_{xy} and π^*_{xz} (see the natural orbitals and their corresponding occupancies in the Supporting Information Tables S19 and S20 and Figures S2−S9) as also found for pure density functional methods.

By contrast, using the B3LYP-optimized geometry a mixed state in between the $^3\Pi_{LS}$ and the $^3\Pi_{HS}$ configurations is obtained with spin density of about 2.4 on Mn and −0.4 on O. As such, the $^3\Pi_{HS}$ state found by hybrid functionals can be attributed to a lack of electronic correlation of the Hartree−Fock orbitals.

DFT-optimized geometries were used as the input geometry for NEVPT2:CAS single-point energy calculations because the system of interest is too large to be optimized at that level of theory. Both NEVPT2:CAS and pure density functional methods find the singlet spin state of $[Mn(O)(H_8Cz)(CN)]^-$ to be the ground state and use optimized geometries that match the experimentally determined ones by the EXAFS methods excellently.[14a] However, in order to determine the variation in singlet−triplet energy levels, we did an additional set of calculations on the lowest lying singlet and triplet spin states with variable Mn−O distances. Thus, we performed constrained surface scans using NEVPT2:CAS along the Mn−O bond using B3LYP relaxed geometries. As can be seen from Figure 1, such constraints should give insight into the adiabatic and diabatic spin state ordering with varying Mn−O distance. The singlet spin state stays the ground state as the Mn−O bond stretches from 1.50 to 1.75 Å, consistent with the spin state ordering predicted by pure density functional methods as well
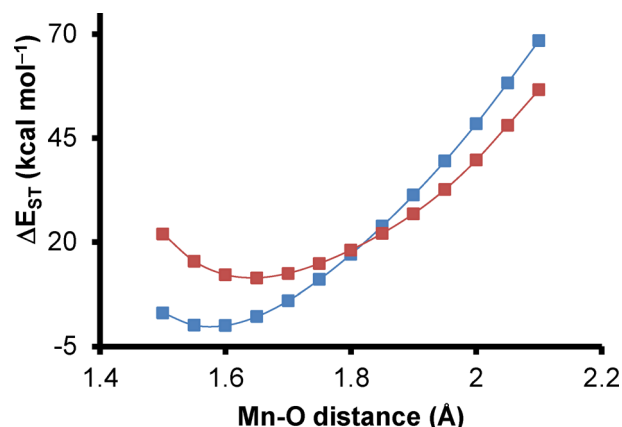

Figure 1. Constrained potential energy scan along the Mn−O bond of $[Mn(O)(H_8Cz)(CN)]^-$ calculated by NEVPT2:CAS(8,7) with BS5. Singlet scans are shown in blue solid squares. Triplet scans are shown in red solid squares. Energies are shown relative to the minimum of the singlet complex for clarity.

as B3LYP. At 1.55 Å, the singlet spin state is the ground state and resides at the minimum point of the singlet PES. At 1.65 Å, the singlet spin state is still the ground state while triplet spin state resides at its minimum point of the triplet PES, consistent with the geometries optimized for the singlet and triplet manganese−oxo species. The triplet and singlet spin states become near-degenerate in the range between 1.75 and 1.85 Å with a spin population of ~2.4 on Mn and ~−0.4 on O. This distance is in line with Mn(IV) species reported in the literature[35] and is the operating bond length during the transition states (vide infra). The triplet spin state becomes the ground state at 1.9 Å in favor of the singlet spin state by ~4 kcal mol^{-1} with a spin population of 2.5 on Mn and −0.6 on O. At 2.1 Å, the spin population is 2.7 on Mn and −0.8 on O. Therefore, the scan along the Mn−O bond distance confirms that a fully optimized NEVPT2 structure would lie in a low-spin ground state, with a significant singlet−triplet energy gap.

The calculations presented here implicate that multireference techniques including NEVPT2 and CASSCF propose the $[Mn(O)(H_8Cz)(CN)]^-$ system to be in a closed-shell singlet ground state. However, its separation from the nearest triplet spin state is considerably larger than previously thought and of the order of 8−10 kcal mol^{-1}, which is at a thermally inaccessible level at room temperature. In addition, the singlet−triplet transition from $^1A_{LS}$ to $^3\Pi_{HS}$ requires a double electron excitation, one from δ_{xy} to π^* and one from π to π^*. As such, this is a spin-forbidden process and may not proceed with a large probability. Moreover, the spin distribution gives a slightly favorable $^3\Pi_{LS}$ state over alternative triplet spin states. The only exception came from the CASSCF spin distribution calculated on top of B3LYP-optimized geometry, which features an unusually long Mn−O distance at 1.78 Å. However, surface scans along the Mn−O bond by NEVPT2:CAS rule out the B3LYP-optimized geometry residing on the minimum of the triplet potential surface of $^3\Pi_{LS}$. B3LYP optimization very likely converged to the higher excited state, the $^3\Pi_{HS}$, of the triplet state, as evidenced by the corresponding spin populations, owing to the lack of electron correlation from the HF exchange parameters.

The pure density functional methods better reproduce the singlet−triplet energy gap found by NEVPT2:CAS compared to the hybrid methods. The spin populations found by
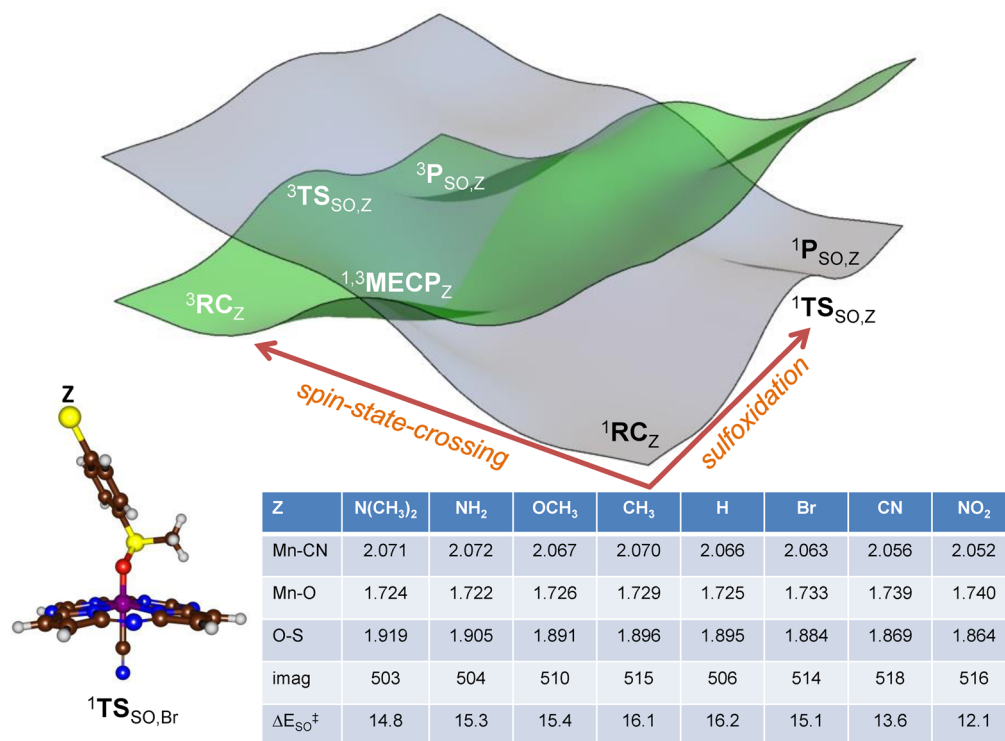
Figure 2. Potential energy landscape for the sulfoxidation of para-Z-substituted thioanisole (SubZ, Z = $N(CH_3)_2$, NH_2, OCH_3, CH_3, H, Br, CN, and NO_2) by $^{1,3}[Mn(O)(H_8Cz)(CN)]^-$. The table gives relative energies (ΔE_{SO}) for $^1TS_{SO}$ as calculated with basis set BS2 and given in kcal mol^{-1}. Optimized geometries of $^1TS_{SO}$ give bond lengths in Angstroms and the imaginary frequency of the transition state in cm^{-1}. **RC** is the reactant complex, **TS**$_{SO}$ is the sulfoxidation transition state, **P**$_{SO}$ is the sulfoxide product complex, and **MECP** refers to the minimum energy crossing point between the singlet and the triplet spin state.

Z	$N(CH_3)_2$	NH_2	OCH_3	CH_3	H	Br	CN	NO_2
Mn–CN	2.071	2.072	2.067	2.070	2.066	2.063	2.056	2.052
Mn–O	1.724	1.722	1.726	1.729	1.725	1.733	1.739	1.740
O–S	1.919	1.905	1.891	1.896	1.895	1.884	1.869	1.864
imag	503	504	510	515	506	514	518	516
$\Delta E_{SO}^{\ddagger}$	14.8	15.3	15.4	16.1	16.2	15.1	13.6	12.1

NEVPT2:CAS are reproduced well with a BLYP single point on a geometry optimized with a hybrid density functional method. We, therefore, studied the sulfoxidation of para-Z-substituted thioanisoles mediated by $[Mn(O)(H_8Cz)(CN)]^-$ at different spin states by BLYP and TPSSh on B3LYP-optimized geometries. B3LYP is used for geometry optimization due to its success in reproducing experimental rate constants in the literature.[36] TPSSh is also used for reaction energetics for the fact that it is the only hybrid functional that matches the spin state ordering found by NEVPT2:CAS and is the highest rank on the Jacob's ladder scheme among the functionals tested in the section above. As such, the procedure that is used in the following represents a geometry optimization at the B3LYP-D3 level of theory followed by a single-point calculation using BLYP or TPSSh to obtain more reliable spin state energetics.

Calculated Hammett Plots for the Reaction of $[Mn(O)(H_8Cz)(CN)]^-$ with Thioanisole Derivatives. In previous work, our groups have shown that $[Mn(O)(H_8Cz)(CN)]^-$ reacts with para-Z-substituted thioanisoles efficiently.[14a] The experimentally determined plot of the logarithms of the rate constants of para-Z-substituted versus para-H-substituted thioanisole reactions, i.e., $\log(k_Z/k_H)$, did not give a linear correlation with the Hammett constant (σ_p) of the substituent but rather a "V-shaped" Hammett correlation, Scheme 1. It was proposed that different reaction mechanisms were operative, depending on the nature of the substituent. In particular, it was suggested that an electrophilic attack by the metal–oxo group took place with substrates with electron-donating substituents to give a negative Hammett slope, whereas a nucleophilic attack occurred with substrates with electron-withdrawing substituents instead.[14a] Interestingly, the

axially vacant five-coordinated $Mn^V(O)(TBP_8Cz)$ species did not react with any of the para-Z-substituted thioanisoles within a measurable time, and hence, a considerable rate enhancement is observed upon binding of the axial ligand.[14b] Our work as well as that of Fujii and co-workers[37] showed computationally that such a drastic rate enhancement tracked with the increased stability of the product Mn(III) complex, and this thermodynamic driving force extended into the transition state through the Bell–Evans–Polanyi principle. Clearly, a nonlinear Hammett plot would correspond to a change in reaction mechanism between substrates with electron-donating and electron-withdrawing para substituents. We calculated the substrate sulfoxidation of para-Z-substituted-thioanisole (Z = $N(CH_3)_2$, NH_2, OCH_3, CH_3, H, Br, CN, and NO_2) with $^{1,3}[Mn(O)(H_8Cz)(CN)]^-$. Figure 2 displays the calculated potential energy profiles for substrate sulfoxidation by $^{1,3}[Mn(O)(H_8Cz)(CN)]^-$, with structural and energetic values for all $^1TS_{SO,Z}$ geometries. The singlet spin barriers range from 12.1 to 16.2 kcal mol^{-1} for the substrates studied here. All data for the other intermediates, transition states, and products can be found in the Supporting Information (Tables S7–S13). The sulfoxidation reaction is concerted via a single oxygen insertion transition state **TS**$_{SO}$ from a reactant complex (**RC**) and leading to products **P**$_{SO}$. These labels are given the subscript for the Z substituent for the para-Z-substituted thioanisole substrate used. The mechanism follows previously reported substrate sulfoxidation reactions by analogous chemical systems.[38] In all cases, the isolated reactants and reactant complexes are in a closed-shell singlet ground state, and as such the spin state ordering does not change upon the formation of an oxidant–substrate complex **RC**. However, $^1TS_{SO,Z}$ is found to be higher

in energy than $^3TS_{SO,Z}$ in all cases and so is the ordering of the product complexes. To confirm the spin state ordering and find the energy splitting of the two transition states, we ran NEVPT2:CAS(8,7) single points on the optimized geometries of $^{1,3}TS_{SO,NO2}$. These calculations establish that the triplet spin barrier is 4.3 kcal mol^{-1} lower in energy than the singlet spin state. Furthermore, at the NEVPT2:CAS(8,7) level of theory $^3TS_{SO,OCH3}$ had a barrier of 11.8 kcal mol^{-1} relative to the reactant complex, which is not dramatically different from the values obtained at RIJCOSX-TPSSh-D3/def2-QZVPP/ZORA//RIJCOSX-B3LYP-D3/SDD/6-31G(d). As such, the barrier heights displayed in Figure 2 match the NEVPT2:CAS-(8,7) and experimental values well. Moreover, the high-level NEVPT2:CAS(8,7) calculations implicate a much smaller singlet−triplet energy gap in the transition states as initially thought, whereas the gap is considerable in the reactant complexes.

The potential energy landscape covering the two spin states for substrate sulfoxidation by $[Mn(O)(H_8Cz)(CN)]^-$ is schematically depicted at the top of Figure 2. This mechanism is the same for all substrates investigated here. Thus, there is a substrate sulfoxidation mechanism from isolated reactants via **RC** and **TS$_{SO}$** leading to products on the singlet spin state (gray surface), and there is an analogous pathway on the triplet spin state (green surface). A 3D representation of the potential energy surface is shown in Figure 2, where the two surfaces are bisected on a spin crossing line, with the lowest energy crossing point the minimum energy crossing point (MECP). The spin transition from singlet to triplet is located on the axis to the left. Thus, the spin crossing seam will have a MECP, where the singlet and triplet energies overlap. As such the landscape will follow a bifurcation pathway, whereby one pathway from singlet spin reactants will directly lead to sulfoxide products via $^1TS_{SO}$, whereas the alternative pathway will proceed via a spin crossover via $^{1,3}MECP$ to the triplet spin state surface followed by sulfoxidation through $^3TS_{SO}$ en route to products.

To find out whether the singlet and triplet spin state surfaces cross and could lead to a spin state change along the reaction mechanism, we calculated minimum energy crossing points (MECP) for the singlet to triplet transitions using the procedures of Harvey.[39] Thus, our MECP-calculated singlet−triplet crossing points give chemical structures (see Figure 3) that do not lie on the substrate sulfoxidation reaction pathway. In particular, the sulfur atom of the substrate is oriented away from the terminal oxo ligand, and there is no S−O bond formation. Instead, the MECP structures show a weak (hydrogen bonding) interaction between substrate and oxidant with the protons of the methyl and phenyl groups of the
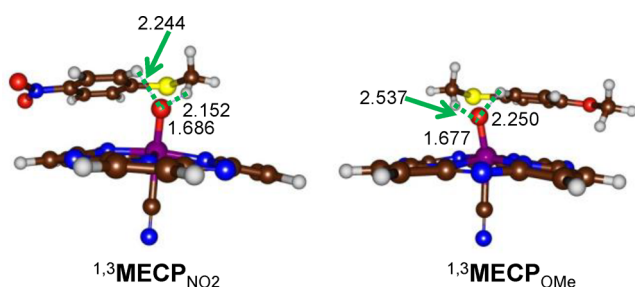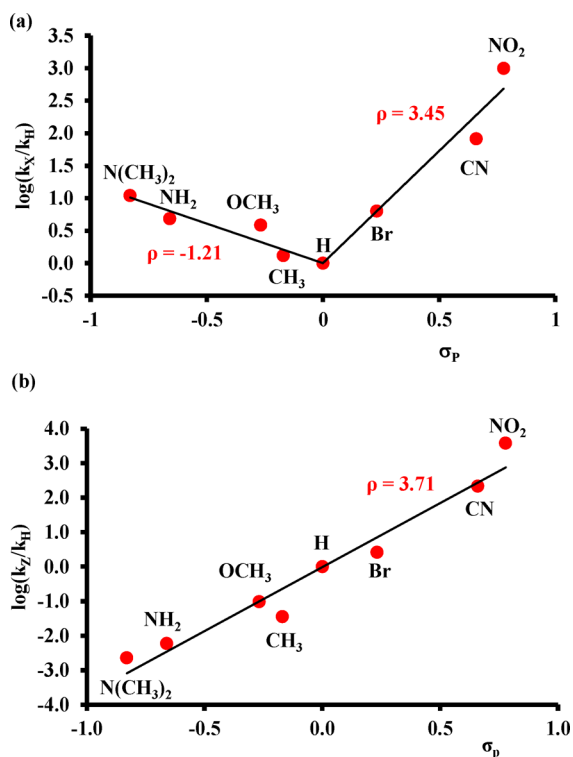
substrate forming nonbonding interactions with the oxo ligand. The singlet−triplet crossing does not appear to happen along the sulfoxidation mechanism but rather occurs as a spin state crossover in the reactant complexes.

The $^{1,3}MECP$ structures have long Mn−O distances of well over 1.67 Å and resemble the triplet spin reactants. Our MECP-calculated crossing points are approximately 4−5 kcal mol^{-1} higher in energy than ^1RC_Z and correspond to a triplet spin state with about two unpaired electrons on the MnO unit. Recall that in the reactant structures a singlet−triplet energy gap of 8 kcal mol^{-1} was obtained using the highest level of theory, and, hence the real crossing points may be well higher than that. Therefore, upon elongation of the Mn−O bond similarly to the scan in Figure 1, the surface crossing is reached. These MECP structures can lead to a singlet−triplet crossing during the lifetime of the reactant complexes but may not connect to the sulfoxide products and/or transition states. In the event of long-lived reactant complexes a thermal Boltzmann equilibration may populate the triplet spin state and lead to reactivity with sulfides on the lower energy surface. However, based on the energetic separation by the singlet and triplet spin state as calculated with NEVPT2:CAS, we expect the thermal occupation of the triplet spin state to be very small.

Key bond lengths of the optimized low-spin transition state structures $^1TS_{SO,Z}$ are given in Figure 2. As follows for the series Z = N(CH$_3$)$_2$ to Z = NO$_2$ the Mn−CN distance gradually decreases from 2.071 to 2.052 Å, while the Mn−O distance elongates from 1.724 to 1.740 Å in an almost linear fashion. At the same time the O−S distance decreases from Z = N(CH$_3$)$_2$ to Z = NO$_2$ from 1.919 to 1.864 Å. These trends imply that an electron-withdrawing substituent, such as NO$_2$, gives transition states with structures that are later on the potential energy surface (shorter S−O bonds) than substrates with electron-donating substituents, in agreement with what was observed previously on analogous systems.[40] All transition states are characterized with a single imaginary mode for the S−O bond formation with values in the range of i503−i518 cm^{-1}.

The Hammett correlation for the enthalpy of activation of para-Z-substituted thioanisole in reaction with $[Mn(O)-(H_8Cz)(CN)]^-$ versus σ_P for the singlet and triplet spin sulfoxidation barriers is shown in Figure 4. The values of $\log(k_Z/k_H)$ were estimated from the enthalpies of activation, see Supporting Information for details. The computations reproduce experiment well *for the singlet spin state only*, giving a "V-shaped" Hammett plot, regardless of the choice of functionals and basis sets, although the calculations give a slightly earlier mechanistic switch from Z = Br to Z = H with respect to experiment. In particular, the triplet spin barriers give a linear correlation between the Hammett σ_P value and $\log k_Z/k_H$ for the full set of substrates tested in the range from $\sigma_P = -0.83$ (Z = (N(CH$_3$)$_2$) to $\sigma_P = +0.778$ (NO$_2$). Clearly, the experimentally determined V-shaped Hammett plot cannot correspond to rate constants obtained through the triplet spin pathway. These results also imply that the spin state crossing from singlet to triplet before the rate determining step is unlikely, in line with the conclusion reached from the low spin−orbit coupling constants.

As computational trends often give a systematic error with respect to experiment as shown before, they do tend to correctly reproduce regio- and chemoselectivities of reaction[41] as well as product isotope effects.[42] In particular, the computation gives a somewhat wider energy gap between the enthalpy of activation of the para-Z substituted thioanisoles

Figure 3. MECP-optimized geometries for the singlet−triplet transition for $[Mn(O)(H_8Cz)(CN)]^-$ with p-NO$_2$-thioanisole and p-OCH$_3$-thioanisole. Bond lengths are given in Angstroms.

Figure 4. Computational Hammett plot for the reaction of singlet and triplet $[Mn(O)(H_8Cz)(CN)]^-$ with para-Z-substituted thioanisole derivatives. Data calculated at RIJCOSX-TPSSh-D3/def2-QZVPP/ZORA//RIJCOSX-B3LYP-D3/SDD/BS2 and includes zero-point, thermal, and solvent corrections. (a) Correlation for singlet spin barriers ($^1TS_{SO,Z}$). (b) Correlation for triplet spin barriers ($^3TS_{SO,Z}$).

with respect to the experimental trends. As a consequence, the Hammett ρ values are larger than those reported in ref 14a. The deviation between experimental and computational rate constants may have to do with the incorrect description of solvent and neglecting entropic and thermal corrections in the calculations.

Technically, the transition state can also exist in a triplet and quintet spin state, and therefore, we calculated the trends for sulfoxidation reactions on those spin states and show the results in Figures 4b and S1. The calculated relative energies from DFT for the triplet and quintet spin states give a good match to those obtained from the NEVPT2:CAS(12,11) calculations. However, despite the fact that the triplet and quintet barriers have structural similarities to the singlet spin state transition states, no mechanistic switch was observed when the rate constant ratio $\log(k_Z/k_H)$ was plotted against the Hammett parameter. For the full set of substrates, a linear trend with positive slope was found. The calculated Hammett plots for the triplet and quintet spin states do not match with experiment, indicating that these barriers cannot be the rate-determining step in the reaction mechanism. These findings also suggest that the spin–orbit coupling for the singlet–triplet transition is small, and little or no conversion from singlet to triplet takes place during the lifetime of the reactant complexes. We conclude that the reaction most likely takes place on a dominant singlet spin state surface. There is a spin state crossing to a more stable spin state only after passing the transition state, and this crossing then happens through thermal equilibration of product complexes, forming a final quintet spin Mn(III) product as experimentally observed.[12,13] To confirm

these results, the spin–orbit coupling (SOC) constants for all systems were calculated (Table 3). Values ranging from 2.9

Table 3. Spin–Orbit Coupling at the Triplet Transition States of Sulfoxidation of Different Para-Z-Substituted Thioanisoles by $[Mn(O)(H_8Cz)(CN)]^-$ (values in cm^{-1})

| Z	OCH$_3$	CH$_3$	H	Br	CN	NO$_2$
SOC	2.9	3.3	3.7	5.0	3.9	3.6

cm^{-1} for p-OCH$_3$-thioanisole to 5.0 cm^{-1} for p-Br-thioanisole are found. These SOC values are very small and implicate little or no spin state change, and the highest reaction probability will lie on the low-spin surface. These give further support for single-state reactivity on the low-spin state.

As shown above, the substrate sulfoxidation reaction by manganese(V)–oxo corrolazine complexes is dependent on the axial ligand bound to the manganese center and on the para-Z-substituent of the thioanisole substrate. In the following we will analyze the properties associated with these trends in detail.

Influence of the Axial Ligand on Reactivity Patterns. As seen in studies on manganese(V)–oxo corrolazine complexes reported previously,[12,14] as well as heme and nonheme iron systems,[43,44] the axial ligand can affect the reactivity properties of metal–oxo complexes dramatically. In particular, an electron-donating or electron-withdrawing axial ligand can influence the electron affinity of the oxidant and/or the pK_a of the oxo group and thereby affect the reactivity patterns and regioselectivity distributions as seen before, for instance, in P450 chemistry.[45] In order to generalize and understand the axial ligand effects we set up a thermochemical cycle as shown in Scheme 3.

Scheme 3. Thermochemical Reaction Scheme Highlighting Ligand Binding versus Oxygen-Atom Transfer
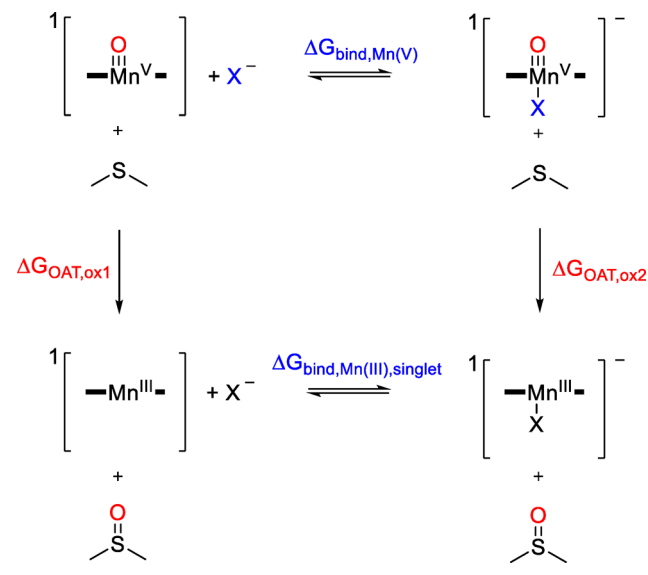
The top reaction in Scheme 3 represents the binding equilibrium of an axial ligand to the manganese(V)–oxo corrolazine with free energy difference $\Delta G_{bind,Mn(V)}$. The bottom reaction, by contrast, represents the binding equilibrium of an axial ligand to a singlet spin manganese(III) corrolazine complex with free energy difference $\Delta G_{bind,Mn(III)}$. The oxygen-atom transfer (OAT) reaction on the singlet spin
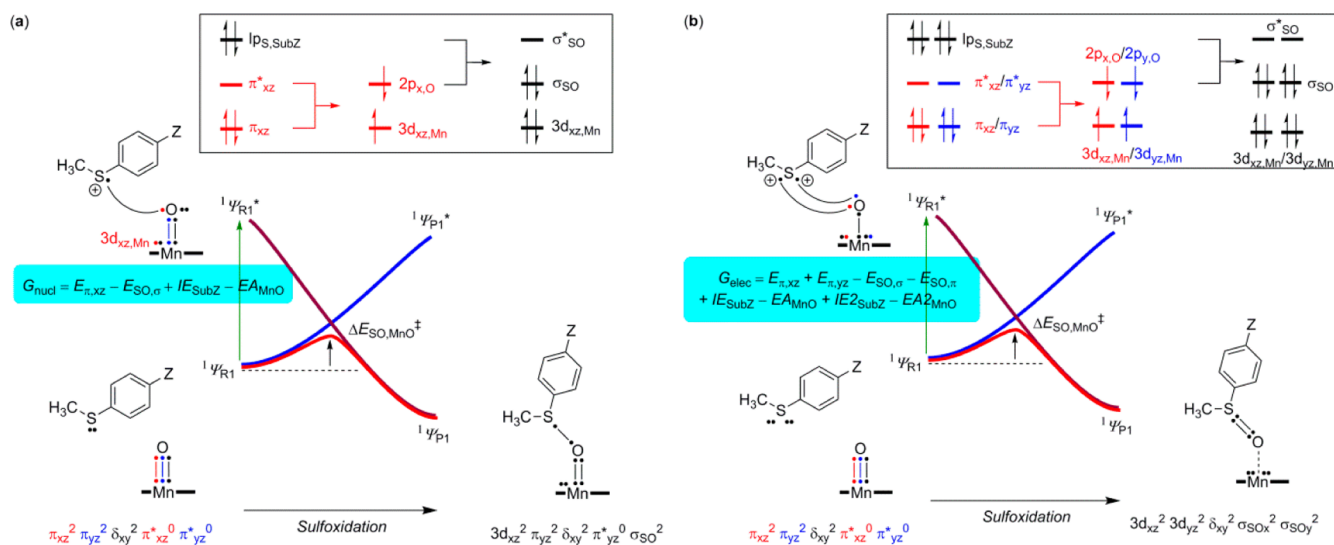
Figure 5. VB curve crossing diagram for nucleophilic and electrophilic sulfoxidation reactions. For explanations see text.

state will lead to singlet spin manganese(III) products. However, the singlet spin manganese(III) products can convert to the more stable quintet spin products afterward through thermal collisions. The two vertical reactions in Scheme 3 describe the OAT reactions of thioanisole with $[Mn^V(O)(H_8Cz)]$ (left) and $[Mn^V(O)(H_8Cz)(X)]^-$ (right), which have an overall driving force of $\Delta G_{OAT,ox1}$ and $\Delta G_{OAT,ox2}$, respectively. Thus, for the Born cycle in Scheme 3, the sum of the four free energy values will be zero, eq 1.

$$\Delta G_{bind,Mn(V)} + \Delta G_{OAT,ox2} - \Delta G_{bind,Mn(III)} - \Delta G_{OAT,ox1}$$
$$= 0 \qquad (1)$$

Therefore, the change in binding strength of an axial ligand to a manganese(V)−oxo versus a manganese(III) center will be equal to the free energy change of sulfoxidation between the axially ligated and the nonaxially ligated complexes, eq 2.

$$\Delta G_{bind,Mn(V)} - \Delta G_{bind,Mn(III)} = \Delta G_{OAT,ox1} - \Delta G_{OAT,ox2} \qquad (2)$$

If we assume that the driving force change between $[Mn(O)(H_8Cz)]$ and $[Mn(O)(H_8Cz)(X)]^-$ is proportional to the free energy of activation change then based on transition state theory we can replace the OAT driving forces with the reaction rates for the oxidation reactions and essentially the rate enhancement k_{ox1}/k_{ox2}. The correlation between axial ligand binding strength and rate enhancement with R being the gas constant and T the actual temperature is given in eq 3. Consequently, the stronger the binding strength difference between the four-coordinate manganese(III) and five-coordinate manganese(V)−oxo complex, the stronger will be the rate enhancement for substrate activation. This conclusion was observed and reported by Fujii earlier.[46]

$$\Delta G_{bind,Mn(V)} - \Delta G_{bind,Mn(III)} \propto RT \ln k_{ox2}/k_{ox1} \qquad (3)$$

In order to test our hypothesis, we calculated the binding strength of axial ligands to manganese(III) and manganese(V)−oxo corrolazine. With X = CN^-, we calculated an axial ligand bond strength difference between the manganese(V)−oxo and the manganese(III) complexes of $\Delta G_{bind,Mn(V)} - \Delta G_{bind,Mn(III)} = 48.4$ kcal mol^{-1}. If we assume a correlation factor of 1.6 for eq 3 based on Marcus theory,[47] this would

correspond with a rate enhancement k_{ox2}/k_{ox1} of 4×10^7 for oxygen-atom transfer. Indeed, no reactivity was observed for thioanisoles with $[Mn(O)(H_8Cz)]$ in agreement with a considerably slower reaction rate as compared to the $[Mn(O)(H_8Cz)(CN)]^-$ system.[14a] We further attempted to predict the rate enhancement of alternative complexes with X = F^-, N_3^-, OCN^-, and NO_3^-, see Supporting Information (Tables S23 and S24). We find similar rate enhancements of $[Mn(O)(H_8Cz)X]$ with X = CN^-/F^- in agreement with experimental rate enhancements measured for 9,10-dihydroanthracene dehydrogenation by $[Mn(O)(H_8Cz)(X)]^-$.[12] The studies also show that much lower rate enhancements may be expected for manganese(V)−oxo corrolazine complexes with N_3^-, OCN^-, and NO_3^- ligands, since these are much weaker bound ligands. In particular, an N_3^-, OCN^-, or NO_3^- ligand binds much weaker to the Mn^{III} complex, and therefore, their rate enhancements are not as dramatic as with F^- and CN^- that see major differences in the binding strength between the Mn^{III} and the $Mn^V(O)$ complexes.

Valence Bond Modeling of Reactivity Patterns. Valence bond curve-crossing diagrams have been used extensively to rationalize reactivity patterns of iron(IV)−oxo oxidants with substrates.[48] These studies explained why the reactions were stepwise and also identified the electrochemical and thermochemical properties of oxidant and substrate that drive the reaction. The VB curve-crossing diagrams give a rationalization of the electronic changes to oxidant and substrate during the oxygen-atom transfer process. Figure 5 gives the two VB diagrams representing the nucleophilic and electrophilic reaction pathways for thioanisole sulfoxidation by $[Mn^V(O)(H_8Cz)(CN)]^-$.

The landscapes start on the bottom-left with the reactant complexes, which are manganese(V)−oxo complexes in the closed-shell singlet spin state ($^1A_{LS}$) with orbital occupation [core] $\pi_{yz}^2 \delta_{xy}^2 a''^2$. Key bonds in the VB structures are indicated with two dots separated by a line. In particular, along the Mn−O bond there are interactions due to the π and π^* orbitals for mixing of the metal $3d_{xz}$ and $3d_{yz}$ atomic orbitals with 2p orbitals on the oxo group. The π_{xz}/π^*_{xz} pair of orbitals is depicted in red, while the π_{yz}/π^*_{yz} pair of orbitals is given in blue. The para-Z-substituted thioanisole substrate (SubZ) is located in the vicinity, and one of the sulfur lone pairs is

highlighted with two dots. Upon oxygen-atom transfer some of the bonds break and electrons are migrated between groups as shown in the corresponding VB structures of the two possible product VB wave functions in part a and b. In VB theory, the reactant state connects to an excited state in the sulfoxide product, whereas the product wave function is linked to an excited state of the reactant wave function. Along the reaction pathway the two wave functions cross, leading to an avoided crossing that results in a transition state for the reaction. It has been shown that the excitation energy (G) from the reactant to the product state in the geometry of the reactants, i.e., the energy difference between $^1\Psi_{R1}$ and $^1\Psi_{R1}*$ in Figure 5a, is proportional to the barrier height of the reaction. Therefore, we compare VB structures of the ground and excited state complexes in the geometry of the reactants to ascertain the properties of oxidant and substrate that determine the reactivity.

We consider two possibilities for the reaction mechanism, namely, a nucleophilic and an electrophilic pathway. The nucleophilic pathway is shown in Figure 5a and includes a single bond formation between the substrate and the oxo group. In the process, the $\pi_{xz}/\pi*_{xz}$ pair of orbitals along the Mn−O bond split back into atomic orbitals, i.e., $2p_O$ and $3d_{xz,Mn}$, both with one electron, which will cost the system an amount of energy $E_{\pi,xz}$. The radical in $2p_O$ forms a bond with one electron from the lone pair on sulfur, and the S−O bond formed will have an energy $E_{SO,\sigma}$. The second electron from the lone pair is transferred to the manganese, so that the excitation energy for the nucleophilic mechanism (G_{nucl}) essentially includes the one-electron ionization (IE_{SubZ}) of the substrate and the one-electron reduction of the oxidant (EA_{MnO}) as shown by eq 4.

$$G_{nucl} = E_{\pi,xz} - E_{SO,\sigma} + IE_{SubZ} - EA_{MnO} \qquad (4)$$

The reactant has three sets of bonding orbitals along the Mn−O bond, namely, the $\sigma_{z2}/\sigma*_{z2}$, $\pi_{yz}/\pi*_{yz}$, and $\pi_{xz}/\pi*_{xz}$ pair of orbitals, which formally gives the Mn−O interaction a triple bond of which we highlight the $\pi/\pi*$ pairs in Figure 5a in color. However, upon thioanisole attack the triple bond is converted into a double bond as also seen from the distances displayed in Figure 2 as compared to the much shorter reactant Mn−O distances.

The alternative reaction mechanism would provide us an electrophilic reaction with excitation energy G_{elec}, eq 5. Now the $\pi_{xz}/\pi*_{xz}$ and $\pi_{yz}/\pi*_{yz}$ pair of orbitals revert back into atomic orbitals, and both lone pairs of sulfur form a bond with the two newly generated 2p orbitals on oxygen. In this process the substrate loses two electrons to the metal, so that the G_{elec} value will be proportional to twice the substrate ionization energy plus the first and second reduction energy of the manganese−oxo complex. Of course the S═O bond formed with energy $E_{S═O}$ is now a double bond rather than a single bond in the nucleophilic pathway and is based on the energy to form the σ bond ($E_{SO,\sigma}$) and the energy to form the π bond ($E_{SO,\pi}$).

$$G_{elec} = E_{\pi,xz} + E_{\pi,yz} - E_{SO,\sigma} - E_{SO,\pi} + IE_{SubZ} - EA_{MnO}$$
$$+ IE2_{SubZ} - EA2_{MnO} \qquad (5)$$

To understand the driving force for the switch of trend in the Hammett correlation, one can picture two reaction mechanisms leading to products, namely, those described in Figure 5a and 5b, respectively. Pathway A can be formally described as oxidation of the oxo group by manganese(V) to form

manganese(IV)−oxyl followed by radical coupling between the oxyl radical and sulfur radical into an S−O bond. This pathway will be followed by substrates with electron-withdrawing substituents such as NO2 and compensates for the higher ionization energy of the thioanisole by delaying oxidation of sulfur until later along the mechanism.

To strengthen our hypothesis we evaluated values of G_{nucl} and G_{elec} for all substrates SubZ using eqs 4 and 5 and subsequently converted those to sulfoxidation barrier heights by multiplying with a factor of 1/3.[49] The correlations of these parameters with the Hammett parameter σ_P are shown in Figure 6. Thus, we calculated the one-electron ionization
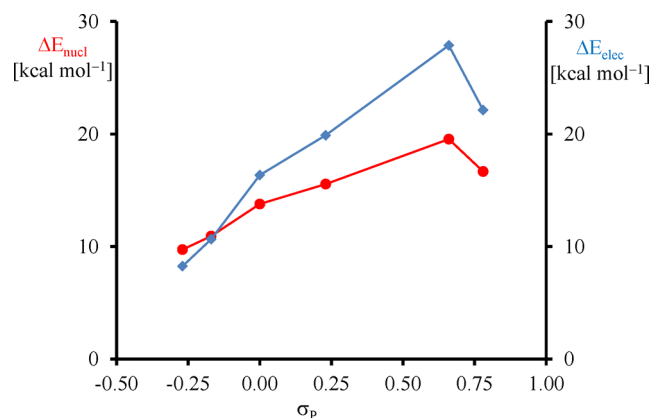
Figure 6. VB predicted values of the barrier heights ΔE_{nucl} and ΔE_{elec} from first principles. Values are in kcal mol^{-1} and plotted against the σ_P Hammett parameter.

energy of all substrates (IE_{SubZ}) and the one-electron reduction of $[Mn(O)(H_8Cz)(CN)]^-$ (EA_{MnO}). In addition, we evaluated the one-electron ionization of the oxidized substrates ($IE2_{SubZ}$) and the one-electron reduction of $[Mn(O)(H_8Cz)(CN)]^{2-}$, i.e., $EA2_{MnO}$.

Then, we took one-half the energy gap between the π_{xz} and the $\pi*_{xz}$ molecular orbitals in the singlet spin state as a measure for $E_{\pi,xz}$ and utilized the same procedure for $E_{\pi,yz}$. Finally, the strength of the σ and π orbitals along the S−O bond was estimated from the energy gap between the $\sigma_{SO}/\sigma*_{SO}$ and the $\pi_{SO}/\pi*_{SO}$ orbitals from the individual isolated product structures. The resulting values of G_{nucl} and G_{elec} for each reaction of $[Mn(O)(H_8Cz)(CN)]^-$ with substrate SubZ (Z = OCH3, CH3, H, Br, CN, and NO2) were calculated and converted into barrier heights and plotted versus the Hammett parameter σ_P of the substrate. As can be seen from Figure 6, the value for ΔE_{nucl} gradually increases from Z = OCH3 to Z = CN but dips slightly for Z = NO2. A similar trend for G_{elec} is found, although the slope is considerably different. As a result, the lowest reaction barrier for Z = OCH3 and Z = CH3 leads to a favorable electrophilic over nucleophilic pathway, whereas for the other substrates a more favorable nucleophilic pathway is predicted. The empirical values used in the valence bond model, therefore, predict reactivity trends in close agreement with those found experimentally even though a slightly earlier change from electrophilic to nucleophilic is found. Consequently, the VB diagram and VB analysis predicts a mechanistic change for substrate sulfoxidation by $[Mn(O)-(H_8Cz)(CN)]^-$ upon replacing the para substituent from a strongly electron-donating group, such as OCH3, to a more electron-withdrawing substituent like CN or NO2. This unique

profile is only found for the singlet spin reaction pathway via $^1\mathbf{TS}_{SO,Z}$ and not found for the triplet spin barriers. Therefore, the change in mechanism from electrophilic to nucleophilic is clear evidence of singlet spin reactivity without crossover to a higher spin state surface. Thus, the experimental Hammett plot represents the first example of proof of singlet spin reactivity originating from a closed-shell singlet manganese(V)−oxo complex.

Finally, note that computational modeling proposed spin-selective reactivity for several examples previously. Thus, substrate sulfoxidation by iron(IV)−oxo porphyrin cation radical complexes generally gives lower barriers on the doublet spin state than on the quartet spin state and thereby gives spin-selective reactivities with different reaction trends.[38,50] Furthermore, aromatic hydroxylation by iron(IV)-oxo porphyrin cation radical models often give spin selective reactivity too, through a rate-determining electrophilic reaction step, whereby two electrons are transferred from substrate to oxidant and hence different barrier heights are found on each spin state surface.[51] As such, these systems may very well give different Hammett plots for substrate sulfoxidaton and aromatic hydroxylation, but future studies will need to be done to establish these details.

CONCLUSION

A series of detailed computational studies has been performed on the reaction mechanism of $[Mn(O)(H_8Cz)(CN)]^-$ with para-Z-substituted thioanisole substrates. A change in reaction mechanism is observed upon changing the para-Z substituent of thioanisoles. Our detailed computational analysis provides evidence that this mechanistic change can only happen on the singlet spin state surface in barrier $^1\mathbf{TS}_{SO,Z}$, whereas no mechanistic change is expected on the triplet spin state surface. The experimental Hammett plot provides a means to identify the reactive spin state of a high-valent manganese−oxo complex and highlights a low-spin reactivity pathway.

A range of density functional and ab initio methods up to the NEVPT2:CAS(12,11) level of theory have been applied and validated against experiment. The NEVPT2:CAS calculations predict well-separated singlet and triplet spin states in the reactant structures by well over $8-10$ kcal mol^{-1}. Although during the reaction mechanism we find close-lying singlet and triplet spin state surfaces with an accessible spin-crossing point lower in energy than the sulfoxidation barriers, actually the spin−orbit coupling constant is very small. Therefore, theory predicts it to be unlikely that a spin state crossing from the singlet to the triplet spin state will take place. The computational rate constants give a V-shaped Hammett plot for para-Z-substituted sulfoxidation reactions only in the case of the singlet surface in agreement with experiment. The mechanism and ligand and substituent effects are rationalized with thermochemical cycles and valence bond theory, which confirm the hypothesis and explain the change in reaction mechanism from nucleophilic to electrophilic.

ASSOCIATED CONTENT

ⓢ Supporting Information

The Supporting Information is available free of charge on the ACS Publications website at DOI: 10.1021/jacs.6b05027.

Computational tables with group spin densities and charges and absolute and relative energies of all

structures discussed here as well as Cartesian coordinates of optimized geometries (PDF)

AUTHOR INFORMATION

Corresponding Authors
*dpg@jhu.edu
*sam.devisser@manchester.ac.uk

Present Address
§School of Chemistry, Cardiff University, Main Building, Park Place, Cardiff CF10 3AT, United Kingdom.

Author Contributions

The manuscript was written through contributions of all authors. All authors have given approval to the final version of the manuscript.

Notes

The authors declare no competing financial interest.

ACKNOWLEDGMENTS

REFERENCES

(1) See, e.g.: (a) Solomon, E. I.; Brunold, T. C.; Davis, M. I.; Kemsley, J. N.; Lee, S. K.; Lehnert, N.; Neese, F.; Skulan, A. J.; Yang, Y. S.; Zhou, J. *Chem. Rev.* **2000**, *100*, 235−349. (b) Bugg, T. D. H. *Curr. Opin. Chem. Biol.* **2001**, *5*, 550−555. (c) Ryle, M. J.; Hausinger, R. P. *Curr. Opin. Chem. Biol.* **2002**, *6*, 193−201. (d) Costas, M.; Mehn, M. P.; Jensen, M. P.; Que, L., Jr *Chem. Rev.* **2004**, *104*, 939−986. (e) Abu-Omar, M. M.; Loaiza, A.; Hontzeas, N. *Chem. Rev.* **2005**, *105*, 2227−2252. (f) Bruijnincx, P. C. M.; van Koten, G.; Klein Gebbink, R. J. M. *Chem. Soc. Rev.* **2008**, *37*, 2716−2744. (g) Kryatov, S. V.; Rybak-Akimova, E. V.; Schindler, S. *Chem. Rev.* **2005**, *105*, 2175−2226.

(2) (a) Ortiz de Montellano, P. R. *Chem. Rev.* **2010**, *110*, 932−948. (b) Guengerich, F. P. *Chem. Res. Toxicol.* **2001**, *14*, 611−650. (c) Munro, A. W.; Girvan, H. M.; McLean, K. J. *Nat. Prod. Rep.* **2007**, *24*, 585−609. (d) Li, D.; Wang, Y.; Han, K. *Coord. Chem. Rev.* **2012**, *256*, 1137−1150.

(3) (a) Meunier, B.; de Visser, S. P.; Shaik, S. *Chem. Rev.* **2004**, *104*, 3947−3980. (b) Denisov, I. G.; Makris, T. M.; Sligar, S. G.; Schlichting, I. *Chem. Rev.* **2005**, *105*, 2253−2277. (c) Rittle, J.; Green, M. T. *Science* **2010**, *330*, 933−937.

(4) (a) Krebs, C.; Galonić Fujimori, D.; Walsh, C. T.; Bollinger, J. M., Jr *Acc. Chem. Res.* **2007**, *40*, 484−492. (b) Nam, W. *Acc. Chem. Res.* **2007**, *40*, 522−531.

(5) (a) Shaik, S.; de Visser, S. P.; Ogliaro, F.; Schwarz, H.; Schröder, D. *Curr. Opin. Chem. Biol.* **2002**, *6*, 556−567. (b) de Visser, S. P.; Ogliaro, F.; Harris, N.; Shaik, S. *J. Am. Chem. Soc.* **2001**, *123*, 3037−3047. (c) de Visser, S. P.; Ogliaro, F.; Sharma, P. K.; Shaik, S. *Angew. Chem., Int. Ed.* **2002**, *41*, 1947−1951.

(6) See, e.g.: (a) Comba, P.; Kerscher, M. *Coord. Chem. Rev.* **2009**, *253*, 564−574. (b) Fukuzumi, S. *Coord. Chem. Rev.* **2013**, *257*, 1564−1575. (c) Ray, K.; Pfaff, F. F.; Wang, B.; Nam, W. *J. Am. Chem. Soc.* **2014**, *136*, 13942−13958. (d) Que, L., Jr; Tolman, W. B. *Nature* **2008**, *455*, 333−340.

(7) (a) Nam, W.; Lee, Y.-M.; Fukuzumi, S. *Acc. Chem. Res.* **2014**, *47*, 1146−1154. (b) McDonald, A.; Que, L., Jr *Coord. Chem. Rev.* **2013**, *257*, 414−428. (c) Ryabov, A. D. *Adv. Inorg. Chem.* **2013**, *65*, 117−163.

(8) (a) Neu, H.; Baglia, R. A.; Goldberg, D. P. *Acc. Chem. Res.* **2015**, *48*, 2754−2764. (b) Chen, Z.; Yin, G. *Chem. Soc. Rev.* **2015**, *44*, 1083−1100.

(9) (a) Usharani, D.; Janardanan, D.; Li, S.; Shaik, S. *Acc. Chem. Res.* **2013**, *46*, 471−482. (b) Holland, P. L. *Acc. Chem. Res.* **2015**, *48*, 1696−1702.

(10) (a) Hirao, H.; Kumar, D.; Que, L., Jr; Shaik, S. *J. Am. Chem. Soc.* **2006**, *128*, 8590−8606. (b) Mandal, D.; Ramanan, R.; Usharani, D.; Janardanan, D.; Wang, B.; Shaik, S. *J. Am. Chem. Soc.* **2015**, *137*, 722−733. (c) Mandal, D.; Shaik, S. *J. Am. Chem. Soc.* **2016**, *138*, 2094−2097.

(11) (a) Liu, H. Y.; Zhou, H.; Liu, L. Y.; Ying, X.; Jiang, H. F.; Chang, C. K. *Chem. Lett.* **2007**, *36*, 274−275. (b) Jin, N.; Ibrahim, M.; Spiro, T. G.; Groves, J. T. *J. Am. Chem. Soc.* **2007**, *129*, 12416−12417.

(12) Prokop, K. A.; de Visser, S. P.; Goldberg, D. P. *Angew. Chem., Int. Ed.* **2010**, *49*, 5091−5095.

(13) Janardanan, D.; Usharani, D.; Shaik, S. *Angew. Chem., Int. Ed.* **2012**, *51*, 4421−4425.

(14) (a) Neu, H. M.; Yang, T.; Baglia, R. A.; Yosca, T. H.; Green, M. T.; Quesne, M. G.; de Visser, S. P.; Goldberg, D. P. *J. Am. Chem. Soc.* **2014**, *136*, 13845−13852. (b) Neu, H. M.; Quesne, M. G.; Yang, T.; Prokop-Prigge, K. A.; Lancaster, K. M.; Donohoe, J.; DeBeer, S.; de Visser, S. P.; Goldberg, D. P. *Chem. - Eur. J.* **2014**, *20*, 14584−14588.

(15) (a) Neese, F. *Comput. Mol. Sci.* **2012**, *2*, 73−78. (b) Frisch, M. J.; Trucks, G. W.; Schlegel, H. B.; Scuseria, G. E.; Robb, M. A.; Cheeseman, J. R.; Scalmani, G.; Barone, V.; Mennucci, B.; Petersson, G. A.; Nakatsuji, H.; Caricato, M.; Li, X.; Hratchian, H. P.; Izmaylov, A. F.; Bloino, J.; Zheng, G.; Sonnenberg, J. L.; Hada, M.; Ehara, M.; Toyota, K.; Fukuda, R.; Hasegawa, J.; Ishida, M.; Nakajima, T.; Honda, Y.; Kitao, O.; Nakai, H.; Vreven, T.; Montgomery, Jr, J. A.; Peralta, J. E.; Ogliaro, F.; Bearpark, M.; Heyd, J. J.; Brothers, E.; Kudin, K. N.; Staroverov, V. N.; Keith, T.; Kobayashi, R.; Normand, J.; Raghavachari, K.; Rendell, A.; Burant, J. C.; Iyengar, S. S.; Tomasi, J.; Cossi, M.; Rega, N.; Millam, J. M.; Klene, M.; Knox, J. E.; Cross, J. B.; Bakken, V.; Adamo, C.; Jaramillo, J.; Gomperts, R.; Stratmann, R. E.; Yazyev, O.; Austin, A. J.; Cammi, R.; Pomelli, C.; Ochterski, J. W.; Martin, R. L.; Morokuma, K.; Zakrzewski, V. G.; Voth, G. A.; Salvador, P.; Dannenberg, J. J.; Dapprich, S.; Daniels, A. D.; Farkas, O.; Foresman, J. B.; Ortiz, J. V.; Cioslowski, J.; Fox, D. J. *Gaussian 09*, Revision C.01; Gaussian, Inc.: Wallingford, CT, 2010.

(16) Sainna, M. A.; Sil, D.; Sahoo, D.; Martin, B.; Rath, S. P.; Comba, P.; de Visser, S. P. *Inorg. Chem.* **2015**, *54*, 1919−1930.

(17) Sainna, M. A.; Kumar, S.; Kumar, D.; Fornarini, S.; Crestoni, M. E.; de Visser, S. P. *Chem. Sci.* **2015**, *6*, 1516−1529.

(18) (a) Becke, A. D. *J. Chem. Phys.* **1993**, *98*, 5648−5652. (b) Lee, C.; Yang, W.; Parr, R. G. *Phys. Rev. B: Condens. Matter Mater. Phys.* **1988**, *37*, 785−789.

(19) (a) Hay, P. J.; Wadt, W. R. *J. Chem. Phys.* **1985**, *82*, 270−283. (b) Hehre, W. J.; Ditchfield, R.; Pople, J. A. *J. Chem. Phys.* **1972**, *56*, 2257−2262.

(20) Grimme, S.; Antony, J.; Ehrlich, S.; Krieg, H. *J. Chem. Phys.* **2010**, *132*, 154104.

(21) Tao, J.; Perdew, J. P.; Staroverov, V. N.; Scuseria, G. E. *Phys. Rev. Lett.* **2003**, *91*, 146401.

(22) Klamt, A.; Schuurmann, G. *J. Chem. Soc., Perkin Trans. 2* **1993**, 799−805.

(23) (a) Becke, A. D. *Phys. Rev. A: At., Mol., Opt. Phys.* **1988**, *38*, 3098−3100. (b) Perdew, J. P. *Phys. Rev. B: Condens. Matter Mater. Phys.* **1986**, *33*, 8822−8824.

(24) Perdew, J. P.; Burke, K.; Ernzerhof, M. *Phys. Rev. Lett.* **1996**, *77*, 3865−3868.

(25) Adamo, C.; Barone, V. *J. Chem. Phys.* **1999**, *110*, 6158−6169.

(26) van Wuellen, C. *J. Chem. Phys.* **1998**, *109*, 392−399.

(27) Pantazis, D. A.; Chen, X. Y.; Landis, C. R.; Neese, F. *J. Chem. Theory Comput.* **2008**, *4*, 908−915.

(28) ftp.chemie.uni-karlsruhe.de/pub/basen.

(29) Hess, B. A.; Marian, C. M.; Wahlgren, U.; Gropen, O. *Chem. Phys. Lett.* **1996**, *251*, 365−371.

(30) (a) Ghosh, A.; Taylor, P. R. *Curr. Opin. Chem. Biol.* **2003**, *7*, 113−124. (b) de Visser, S. P.; Stillman, M. J. *Int. J. Mol. Sci.* **2016**, *17*, 519−544.

(31) (a) de Visser, S. P.; Quesne, M. G.; Martin, B.; Comba, P.; Ryde, U. *Chem. Commun.* **2014**, *50*, 262−282. (b) Sallmann, M.; Kumar, S.; Chernev, P.; Nehrkorn, J.; Schnegg, A.; Kumar, D.; Dau, H.; Limberg, C.; de Visser, S. P. *Chem. - Eur. J.* **2015**, *21*, 7470−7479.

(32) Janesko, B. G. *Int. J. Quantum Chem.* **2013**, *113*, 83−88.

(33) Hull, J. F.; Balcells, D.; Sauer, E. L. O.; Raynaud, C.; Brudvig, G. W.; Crabtree, R. H.; Eisenstein, O. *J. Am. Chem. Soc.* **2010**, *132*, 7605−7616.

(34) de Visser, S. P.; Shaik, S.; Sharma, P. K.; Kumar, D.; Thiel, W. *J. Am. Chem. Soc.* **2003**, *125*, 15779−15788.

(35) Leeladee, P.; Baglia, R. A.; Prokop, K. A.; Latifi, R.; de Visser, S. P.; Goldberg, D. P. *J. Am. Chem. Soc.* **2012**, *134*, 10397−10400.

(36) (a) Postils, V.; Company, A.; Solà, M.; Costas, M.; Luis, J. M. *Inorg. Chem.* **2015**, *54*, 8223−8236. (b) Hirao, H. *J. Phys. Chem. A* **2011**, *115*, 9308−9313.

(37) (a) Prokop, K. A.; Neu, H. M.; de Visser, S. P.; Goldberg, D. P. *J. Am. Chem. Soc.* **2011**, *133*, 15874−15877. (b) Takahashi, A.; Yamaki, D.; Ikemura, K.; Kurahashi, T.; Ogura, T.; Hada, M.; Fujii, H. *Inorg. Chem.* **2012**, *51*, 7296−7305.

(38) (a) Kumar, D.; Sastry, G. N.; de Visser, S. P. *Chem. - Eur. J.* **2011**, *17*, 6196−6205. (b) Kumar, S.; Faponle, A. S.; Barman, P.; Vardhaman, A. K.; Sastri, C. V.; Kumar, D.; de Visser, S. P. *J. Am. Chem. Soc.* **2014**, *136*, 17102−17115.

(39) Harvey, J. N.; Aschi, M.; Schwarz, H.; Koch, W. *Theor. Chem. Acc.* **1998**, *99*, 95−98.

(40) Kumar, D.; Latifi, R.; Kumar, S.; Rybak-Akimova, E. V.; Sainna, M. A.; de Visser, S. P. *Inorg. Chem.* **2013**, *52*, 7968−7979.

(41) (a) Faponle, A. S.; Quesne, M. G.; de Visser, S. P. *Chem. - Eur. J.* **2016**, *22*, 5478−548. (b) Barman, P.; Upadhyay, P.; Faponle, A. S.; Kumar, J.; Nag, S. S.; Kumar, D.; Sastri, C. V.; de Visser, S. P. *Angew. Chem., Int. Ed.* **2016**, *55* (37), 11091−11095.

(42) (a) Kumar, D.; de Visser, S. P.; Shaik, S. *J. Am. Chem. Soc.* **2003**, *125*, 13024−1302. (b) Kumar, D.; de Visser, S. P.; Sharma, P. K.; Cohen, S.; Shaik, S. *J. Am. Chem. Soc.* **2004**, *126*, 1907−1920.

(43) (a) Gross, Z.; Nimri, S. *Inorg. Chem.* **1994**, *33*, 1731−1732. (b) Czarnecki, K.; Nimri, S.; Gross, Z.; Proniewicz, L. M.; Kincaid, J. R. *J. Am. Chem. Soc.* **1996**, *118*, 2929−2935. (c) Song, W. J.; Ryu, Y. O.; Song, R.; Nam, W. *JBIC, J. Biol. Inorg. Chem.* **2005**, *10*, 294−304. (d) Crestoni, M. E.; Fornarini, S.; Lanucara, F. *Chem. - Eur. J.* **2009**, *15*, 7863−7866.

(44) (a) Sastri, C. V.; Lee, J.; Oh, K.; Lee, Y. J.; Lee, J.; Jackson, T. A.; Ray, K.; Hirao, H.; Shin, W.; Halfen, J. A.; Kim, J.; Que, L., Jr; Shaik, S.; Nam, W. *Proc. Natl. Acad. Sci. U. S. A.* **2007**, *104*, 19181−19186. (b) Jackson, T. A.; Rohde, J.-U.; Seo, M. S.; Sastri, C. V.; DeHont, R.; Stubna, A.; Ohta, T.; Kitagawa, T.; Münck, E.; Nam, W.; Que, L., Jr *J. Am. Chem. Soc.* **2008**, *130*, 12394−12407.

(45) (a) de Visser, S. P.; Ogliaro, F.; Sharma, P. K.; Shaik, S. *J. Am. Chem. Soc.* **2002**, *124*, 11809−11826. (b) de Visser, S. P. *Chem. - Eur. J.* **2006**, *12*, 8168−8177. (c) de Visser, S. P.; Latifi, R.; Tahsini, L.; Nam, W. *Chem. - Asian J.* **2011**, *6*, 493−504.

(46) (a) Takahashi, A.; Kurahashi, T.; Fujii, H. *Inorg. Chem.* **2011**, *50*, 6922−6928. (b) Cong, Z.; Kurahashi, T.; Fujii, H. *Angew. Chem., Int. Ed.* **2011**, *50*, 9935−9939.

(47) Mayer, J. M. *J. Phys. Chem. Lett.* **2011**, *2*, 1481−1489.

(48) (a) Shaik, S.; Kumar, D.; de Visser, S. P. *J. Am. Chem. Soc.* **2008**, *130*, 10128−10140. (b) de Visser, S. P. *J. Am. Chem. Soc.* **2010**, *132*, 1087−1097. (c) Kumar, D.; Karamzadeh, B.; Sastry, G. N.; de Visser, S. P. *J. Am. Chem. Soc.* **2010**, *132*, 7656−7667.

(49) Quesne, M. G.; Senthilnathan, D.; Singh, D.; Kumar, D.; Maldivi, P.; Sorokin, A. B.; de Visser, S. P. *ACS Catal.* **2016**, *6*, 2230−2243.

(50) (a) Kumar, D.; de Visser, S. P.; Sharma, P. K.; Hirao, H.; Shaik, S. *Biochemistry* **2005**, *44*, 8148−8158. (b) Vardhaman, A. K.; Barman, P.; Kumar, S.; Sastri, C. V.; Kumar, D.; de Visser, S. P. *Angew. Chem., Int. Ed.* **2013**, *52*, 12288−12292.

(51) (a) de Visser, S. P.; Shaik, S. *J. Am. Chem. Soc.* **2003**, *125*, 7413−7424. (b) Faponle, A. S.; Quesne, M. G.; Sastri, C. V.; Banse, F.; de Visser, S. P. *Chem. - Eur. J.* **2015**, *21*, 1221−1236.